LABORATORY TESTS OF PLANET SIGNAL EXTRACTION IN HIGH CONTRAST IMAGES

Pierre Baudoz[1a], Johan Mazoyer[1], and Raphael Galicher[1]

Laboratoire d'Etudes Spatiales et d'Instrumentation en Astrophysique (LESIA), Observatoire de Paris, CNRS, UPMC Paris 6 and Denis Diderot Paris 7, 5 Place Jules Janssen, 92195 Meudon, France.

Abstract. Understanding the formation, evolution and surprising diversity of exoplanetary system is recognized as one of the few major challenges of current astrophysics. While a large number of planets are discovered thanks to techniques like radial velocity and transits, only a few of them have clear measurements of their atmospheric components. Besides, these latter have been studied on transiting planets with very short orbits. Study of planets at larger separations requires direct imaging, which has enabled detection of a handful of exoplanets. This number will dramatically increase with the arrival in 2013 of SPHERE and GPI instruments that will give access to a large class of self-luminous young exoplanets. Characterization of mature planets or even massive rocky planets is expected for the next generation of planet finders that will be installed on Extremely Large Telescopes (ELT). On ELT, even with Adaptive Optics (AO) working at their best, using smart wavefront sensor and correction strategy, it is expected that the residual speckles in the images will still be a factor 100 brighter than the planet signal. This level composed of slow quasi static speckles not detected by the wavefront sensor and the rapidly varying wavefront errors that cannot be corrected by the AO loop frequency. Solutions are actually studied to calibrate these speckles and make sure that we can differentiate them from planet signal. One of the best solution is to use the signal of focal plane wavefront sensors that can help suppressing the quasi-static speckles but also help to extract the planet signal in the final images. After describing the benefit of focal plane wavefront sensor for data extraction, we will describe our laboratory test bench which uses the Self-Coherent Camera as focal plane wavefront sensor. The principle of the data processing used to extract the planet signal will be presented together with laboratory results on very high contrast images.

1 Introduction

To increase our knowledge of exoplanetary science, the international community has started to simultaneously improve theoretical works and develop dedicated facilities from the ground and from space. High contrast direct imaging has an important role to play in the completion of indirect detection techniques such as transits and radial velocities. Today, a few young planets at large separations have already been detected [1,2] and their characterization is starting. Ultimately, direct detection could allow us to fully characterize the properties of exoplanets, including indications of habitability, and physics and chemistry of their atmosphere. The required contrast capability for exoplanet imaging is the main limitation to discoveries in this field. The first generation of ground-based instruments dedicated to high contrast imaging is currently being developed both in Europe and in North America by large international consortia [3,4]. These instruments are now close to starting operations, with an expected contrast performance better than 10^{-6} to 10^{-7} for detecting young Jupiter-like planets within 0.5 arcsec from their star, well inside the stellar halo.

---

[a] pierre.baudoz@obspm.fr

A large improvement of the performance is mandatory to study lower mass planets like Neptunes or possibly rocky planets. This is one of the key motivation for the future extremely large telescopes (ELT), the dominant infrastructures of tomorrow's optical and infrared astronomy from the ground.The contrasts of the latter planets require a deep understanding of the limitations for high contrast imaging and new technological solutions that can self-calibrate the observations. One solution proposed for the direct planet detection on ELT [5] or on space-based projects [6] is the Self-Coherent Camera (SCC). The SCC is a concept of high contrast imaging instrument [7] that takes benefit from the coherence between the stellar leakage speckles and the stellar light rejected by a coronagraph. This property of coherence is used to measure the electric field in the final focal plane [8] or detect a planet among the speckles by post-processing [7].

We focus our paper on the second use of the SCC. After recalling the principle of the SCC, we describe a simple method to improve the contrast of images by using the SCC fringes. After a brief description of the test bench, we present laboratory results for this post-processing methods.

2 Principle and simplified formalism for the Self-Coherent Camera
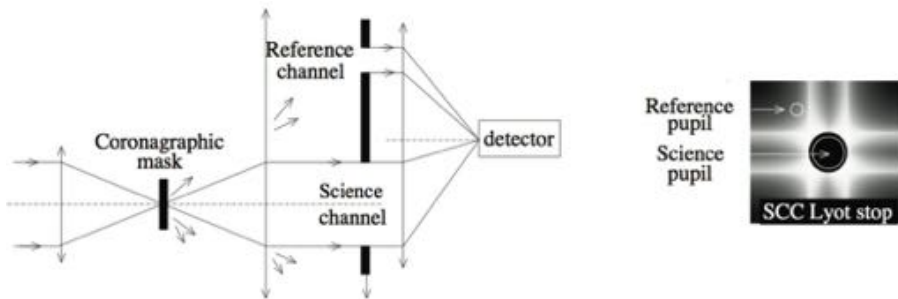
Fig. 1. Principle of the SCC coupled with a Four Quadrant Phase Mask (FQPM) coronagraph [9]. The image on the right shows the light distribution in the pupil plane downstream the coronagraphic focal plane.

A robust design can associate the SCC with most of the coronagraphs by simply modifying the Lyot stop geometry [8]. The principle of the SCC coupled with a Four Quadrant Phase Mask (FQPM) coronagraph [9] is shown in Figure 1. The SCC simply modify the Lyot stop by adding a reference pupil (Figure 1). As in the classical Lyot coronagraph, the star is focalized on a coronagraphic mask. In the pupil downstream of the focal plane mask, an unaberrated stellar light is fully diffracted outside of the pupil geometry. When the beam upstream the coronagraph is aberrated, there is also residual light in the science pupil (classical Lyot stop) that can interfere with light from the reference pupil to create fringed speckles on the detector. Theses fringes can be used to measure the focal plane electric field but also to discriminate speckles from a planet that is not fringed.

Below, we describe briefly the formalism that describes the intensity in the focal plane for a SCC. Following the formalism given in Galicher et al. 2008 and 2010 [8,6], we can write the monochromatic interferential image on the detector I:

$$I(\alpha) = I_P(\alpha) + I_S(\alpha) + I_R(\alpha) + I_-(\alpha) \exp\left(\frac{2i\pi\alpha\xi_0}{\lambda}\right) + I_+(\alpha) \exp\left(\frac{-2i\pi\alpha\xi_0}{\lambda}\right) \tag{1}$$

I_P is the planet contribution in the focal plane. I_S is the intensity of the stellar residual we would get if no reference pupil was added to the Lyot stop in the pupil plane downstream the coronagraph. I_R is the intensity that can be measured if the Lyot stop is occulted. I_- and I_+ are complex functions that are describing the modulated part of the SCC image. α is the focal plane angular coordinate, λ is the wavelength considered and ξ_0 is the distance between the two pupils. $A_S(\alpha)$ directly measures the electric field in the focal plane that we would get with a simple coronagraph.

Defining $A_S(\alpha)$ and $A_R(\alpha)$, the complex amplitudes in the focal plane that propagate through the science pupil and the reference pupil respectively, Equation 1 can also be written

$$I(\alpha) = I_P(\alpha) + |A_S(\alpha)|^2 + |A_R(\alpha)|^2 + A_S(\alpha)A_R(\alpha)^* \exp\left(\frac{2i\pi\alpha\xi_0}{\lambda}\right) + A_S(\alpha)^* A_R(\alpha) \exp\left(\frac{-2i\pi\alpha\xi_0}{\lambda}\right) \quad (2)$$

The modulated parts of $I(\alpha)$ ($I_-(\alpha)$ and $I_+(\alpha)$) are linear functions of the complex amplitudes $A_S(\alpha)$ and $A_R(\alpha)$ and do not depend on the planet contribution:

$$I_-(\alpha) = A_S(\alpha)A_R(\alpha)^* \quad (3)$$

The Fourier transform of an SCC image ($F[I]$, F describing the direct Fourier transform) shows 3 distinct parts if $\xi_0 > 3D/2 + D_R/2$ with D the Lyot diameter and D_R the reference pupil diameter [8,6]. These 3 parts corresponds to the Fourier transform of $I_P + I_S + I_R$ for the central peak and the Fourier transform of I_- and I_+ for the lateral peak.

We can extract the modulated part $I_-(\alpha)$ (or $I_+(\alpha)$) from $I(\alpha)$ by multiplying $F[I(\alpha)]$ by a numerical mask that put to zero every pixels but the one corresponding to $F[I_-(\alpha)]$ in both the real and imaginary part. The diameter of the zone extracted is given by the size of the intercorrelation of the Lyot stop and the reference pupil (theoretical diameter equal to $D_R + D$). Applying an inverse Fourier transform to this image shifted, leads us directly to $I_-(\alpha)$.

We already showed in previous papers that $I_-(\alpha)$ can be used to estimate the electric field in the focal plane $A_S(\alpha)$ and find the shape of the deformable mirror (DM) which minimizes the residual stellar intensity in the coronagraphic focal plane [14,15]. The correction applied to the DM located upstream of the coronagraph creates a dark area called Dark Hole (DH) [11] which is limited to a field of $N\lambda/D \times N\lambda/D$ for a DM with NxN actuators.

However, residual speckles may remain in the focal plane: first outside of the DH and second on one side of the DH if there are amplitude defects [11]. To improve the detection of planets, we can use the fact that the planet is not modulated by fringes while the speckles are, i.e. the planet does not interfere with the light diffracted by the reference pupil.

Since we can extract $I_-(\alpha)$ and $A_S(\alpha)$ from SCC images, we can create a model of image without planet than can be subtracted to our recorded image. Our model image $I^{est}(\alpha)$ is based on Eq. 2 with estimated $A_S^{est}(\alpha)$, $A_R^{est}(\alpha)$, ξ_0^{est}.

$$I^{est}(\alpha) = |A_S^{est}(\alpha)|^2 + |A_R^{est}(\alpha)|^2 + A_S^{est}(\alpha)A_R^{est}(\alpha)^* \exp\left(\frac{2i\pi\alpha\xi_0^{est}}{\lambda}\right) + A_S^{est}(\alpha)^* A_R^{est}(\alpha) \exp\left(\frac{-2i\pi\alpha\xi_0^{est}}{\lambda}\right)$$
$$(4)$$

The term $A_R^{est}(\alpha)$ is based on an image of $I_R(\alpha) = |A_R(\alpha)|^2$ recorded by occulting the lyot stop. Since this image can be noisy, we fit the recorded intensity with a gaussian function $G(\alpha)$ (see Figure 2) . Since the phase of a diffraction pattern for high strehl ratio is not varying [12], we decide to write the estimation of the complex amplitude $A_R(\alpha)$ inside λ/D_R:

3
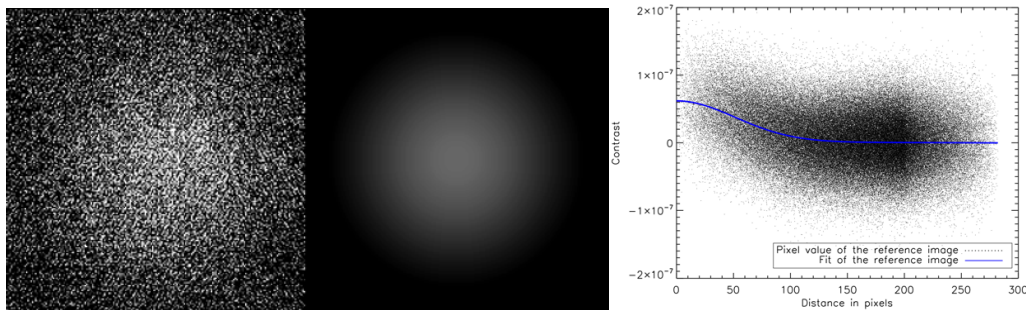
Fig. 2. Left: Recorded image of the reference in the focal plane ($I_R(\alpha) = |A_R(\alpha)|^2$). Center: Estimated image of reference ($|A_R^{est}(\alpha)|^2$). Right: Comparison of the mean profile of $|A_R^{est}(\alpha)|^2$ and the different values taken by the recorded $|A_R(\alpha)|^2$. Narrow spectral bandwidth of 2%

$$A_R^{est}(\alpha) = f_G \sqrt{G(\alpha)} \tag{5}$$

With f_G a coefficient that takes into account possible variation of the reference between the recording of the SCC image and the recording of the reference image. As a result, no detection are practically possible for distance larger than λ/D_R.

The term $A_S^{est}(\alpha)$ is estimated directly from $I_-(\alpha)$. We force the phase of $A_S^{est}(\alpha)$ to be the one recorded by $I_-(\alpha)$ but let the amplitude of $A_S^{est}(\alpha)$ free with an error term $\Delta(\alpha)$:

$$A_S^{est}(\alpha) = \left(\frac{I_-(\alpha)}{A_R^{est}(\alpha)} + \Delta(\alpha) \right) \exp \left[i. \arg \left(\frac{I_-(\alpha)}{A_R^{est}(\alpha)} \right) \right] \tag{6}$$

We simply estimate by hand the distance ξ_0^{est} from the Fourier transform of $I(\alpha)$. Our simple minimization criteria can then be written:

$$J(f_G, \Delta) = \|I(\alpha) - I^{est}(\alpha)\|^2 \tag{7}$$

where $\|x\|^2$ denotes the sum of squared pixel values inside the full DH and where $I^{est}(\alpha)$ is defined by Eq. 4. We minimize J starting with $f_G = 1$ and $\Delta(\alpha) = 0$. Note that the minimization will not be affected by a planet $I_P(\alpha)$ (except by its noise) because it is not modulated. This minimization is rather crude and could be better optimized. However, it already gives encouraging results as shown in Sect. 3.

3 SCC post-processing test bench results

In this section, we are presenting post processing results based on SCC images recorded on the test bench we developed in Laboratoire d'Etudes Spatiales et d'Instrumentation en Astrophysique (LESIA) at Observatoire de Paris. First, we rapidly recall the main characteristics of the bench.

3.1 Test bench description

The test bench is described in details in Mas et al. 2010 [10]. The main components used for the tests presented in this paper are quickly recalled below:

1. An optical fiber source that is fed by a laser diode fiber (@ 635 nm) or a white light source coupled with bandwidth filter (λ = 638nm, $\Delta\lambda$ = 11.3 nm).
2. A fully reflective optical design creating 3 pupil planes where we place:
    (a) An unobscurated entrance pupil plane of 8.1 mm and a tip-tilt mirror
    (b) A Boston Micromachines deformable mirror of 32x32 actuators with a pitch of 0.3 mm. We use only 27x27 actuators to avoid two dead actuators on the DM.
    (c) The Lyot stop of D =8mm (99% filtering) and a reference pupil of D_R =0.35 mm with ξ_0 = 13 mm
3. And 3 focal planes, two of which include:
    (a) A monochromatic Four Quadrant phase mask [9] optimized for 635 nm
    (b) A CCD camera of 640x480 pixels (400x400 used) with a readout noise of 18 e- and a Full Well capacity of 13 000 e-
4. A set of Neutral Density filters to record PSF images (no coronagraph) to normalize the photometry of the coronagraphic images.
5. A software (Labview) that can control the DM to create Dark Holes in the coronagraphic focal plane.

We already presented results of SCC measurements and correction by a DM of the focal plane electric field. The SCC coupled in that case with a Four Quadrant Phase mask coronagraph has already been tested in laboratory environment with monochromatic source [13], as well as with narrow spectral bandwidth (2%, [14]). In the next sections, we will quickly recall these results and use them to test the post-processing method of the SCC.

3.2 Monochromatic results
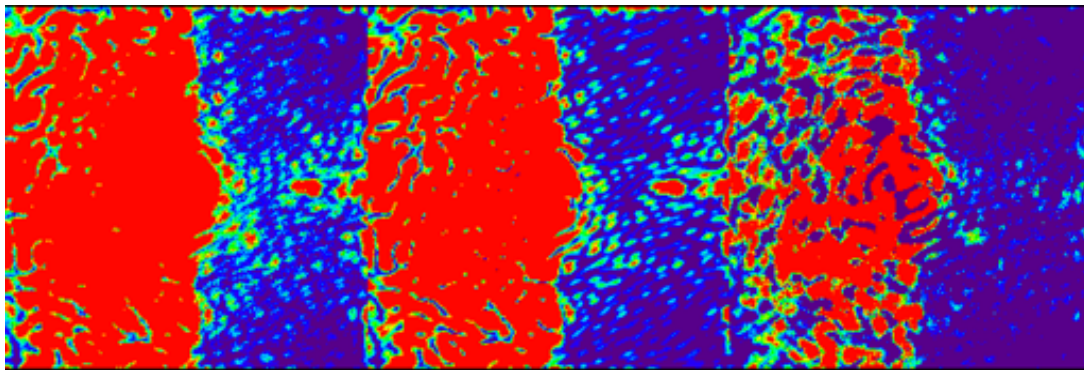
Fig. 3. Left: Recorded image in monochromatic light using correction based on electric field minimization for a half Dark Hole ($I(\alpha)$, Eq. 1). Middle: Estimated image $I^{est}(\alpha)$ reconstructed using Eq. 2, hypotheses and approximations decribed in Sect. 2 . Right: Subtraction image $I(\alpha) - I^{est}(\alpha)$ after post-processing. Same color scale for all images, field of view of 27x27 λ/D for all images .

First, we present the results for monochromatic light. Applying the correction scheme described in [14], we can create a DH inside the focal plane of the SCC image. On our laboratory setup, the full DH of 27x27 λ/D permitted by the DM is limited by amplitude defects [14,15]. To improve the contrast, we need to correct for both phase and amplitude aberations effects in the focal plane. We can do so by limiting the correction to one side of the area that can be corrected by the DM [11], for example a right hand side DH (-13.5 λ/D to +13.5 λ/D in vertical

and 0 λ/D to +13.5 λ/D in horizontal). An example of the minimization of the electric field in such a half DH can be seen in Figure 3 (Left) for monochromatic light. The contrast levels of this image are drawn in Figure 4 (solid lines). We can see in this image that the contrast level is lower than 10^{-7} between 2 and 15 λ/D on the right hand side of the image (solid black line). The Solid blue line corresponds to the contrast on the left hand side which is limited to values between 10^{-5} and 10^{-6} by amplitude aberrations. A numerical simulation taking into account the amplitude defects measured on the bench reaches the same limiting level showing that the correction by the DM is optimized in the context of the minimization of the electric field but also that the SCC is an efficient tool to precisely measure the wavefront defects [14,15]. A second DM would be necessary to remove these speckles [16].

These speckles strongly decrease the performance of the coronagraph on one side of the image. To improve the detection on this side, the solution is to apply the SCC post processing mode that reap the full benefit of the fringes that encode the residual speckles on both sides in the focal plane. To estimate the intensity of the reference image I_R that is needed for this post-processing mode, we occult the Lyot stop and record series of images to minimize the readout noise. The term $A_R^{est}(\alpha)$ is estimated by fitting a gaussian function on I_R as described in Sect. 2. As a result, no improvement of the contrast is expected further than λ/D_R. Thus, we force the outer part of the image (larger than a radius of $20\lambda/D$) to zero.
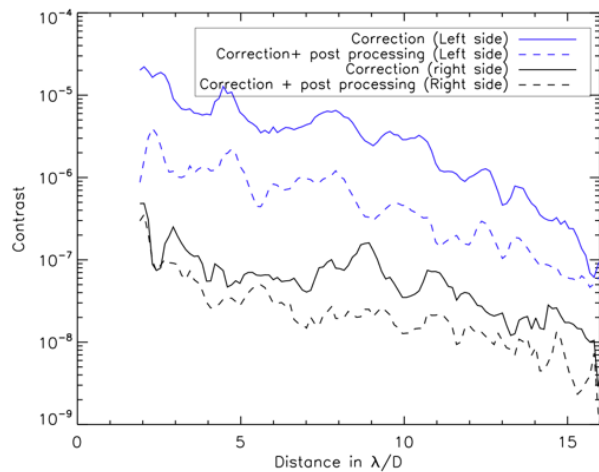
Fig. 4. RMS radial profiles estimated for one-sided DH image for raw correction (solid lines corresponding to Fig. 3, left) and for post-processing (dashed lines corresponding to Fig. 3, right). The profiles are calculated for the left hand side of the image (blue lines corresponding to the side limited by amplitude aberration) and right hand side part of the image(black lines corresponding to the DH side). Monochromatic results.

To quantify the effect of our post-processing method, we compare the radial profiles of the azimutal average estimated before and after applying our post-processing method on both the right and left side of image. In Fig. 4, the solid (dashed) lines correspond to the contrasts reached on SCC images before (after) applying post-processing. The contrast is improved by a factor 10 on the left hand side and about 2-4 on the right hand side. The contrast reaches a value below 10^{-6} all around the star and about $2\ 10^{-8}$ in the DH for angular distances larger than 5 λ/D. The small improvement on the right hand side may be limited by the readout noise (around 10^{-8} RMS).

3.3 Narrow spectral bandwidth results
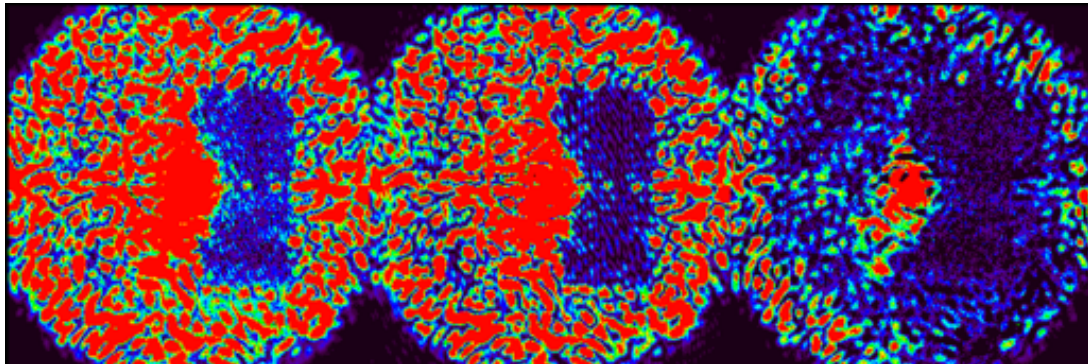
Fig. 5. Same caption than Fig. 3 but for narrow spectral bandwidth (2%)

We also tested the SCC correction with a narrow spectral bandwidth (2%) [14]. The source is fainter than the laser diode. Thus, the signal to noise ratio on a given recorded image is lower than on monochromatic images and the correction is stopped when the one-sided DH is limited by camera readout noise (Fig. 5, left). The contrast achieved in the DH for this image between $5\lambda/D$ and $13\lambda/D$ is between 10^{-7} and $2\ 10^{-7}$ (black solid line in Fig. 6) while the contrast on the left hand side is between 10^{-5} and 10^{-6} (blue solid line in Fig. 6). As in Sect. 3.2, the effects of the amplitude defects strongly decrease the performance of the coronagraph on one side of the image.
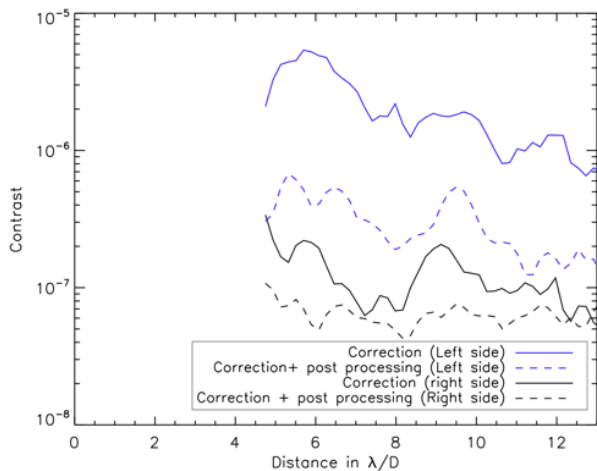
Fig. 6. Same radial profiles than in Fig. 4 but related to the narrow spectral bandwidth (2%) images shown in Fig. 5.

Applying the procedure described in Sect. 2, we can improve the overall contrast in the image as shown in Fig. 5 where the left image corresponds to the DH correction only while the right image shows with the same scale the same image after post-processing. As previously, we estimate the term $A_R^{est}(\alpha)$ by fitting a gaussian function on I_R as described by Equation 5. We also apply the zero-ponderation on the image at distance larger than a radius of $20\lambda/D$ to avoid the division by $A_R^{est}(\alpha)$ in Equation 6 to reach too small values. We can clearly see this ponderation on the three images in Fig. 5.

The contrast is improved by a factor 20 on the left hand side and about 2 on the right hand side. The contrast reaches a value below 10^{-6} all around the star (dashed line in Fig. 6) and about $8\ 10^{-8}$ in the DH between 4 and 13 λ/D (diamond curve in Fig. 6). The small improvement on the right hand side is certainly partly limited by the readout noise level that is estimated for this image at $4\ 10^{-8}$ RMS. Note that the level of noise is estimated after applying the same Fourier filtering on the image than the one automatically applied when calculating $I^{est}(\alpha)$. Indeed, $I^{est}(\alpha)$ is based on the estimation of $A_S^{est}(\alpha)$ (Eq.6) that depends on $I_-(\alpha)$ which is filtered in the Fourier plane by a numerical mask (see the steps used to measure $I_-(\alpha)$ and described in Sect. 2). Even though the left hand side is not perfectly cleaned by the post-processing, the improvement is good enough to enable the detection over the complete DH at a level of a few 10^{-7}. A more symmetrical contrast is very useful not only for improving planet detection strategy but also to image complex structures like faint exozodiacal disks.

3.4 Conclusion

We presented recorded images using the Self-Coherent Camera coupled with a Four Quadrant Phase mask coronagraph and working in laboratory environment with monochromatic source, as well as with narrow spectral bandwidth (2%). Minimizing the electric field in the focal plane enables us to reach contrast level lower than 10^{-7} between 5 and 13 λ/D. We showed that the fringes that encode the speckles are a useful tool to improve further the contrast. We proposed an SCC post processing method and applied it on the recorded data. It helped to improve the contrast by a factor 10 to 20 on the side of the image limited by the amplitude defects. On the DH side, a more modest improvment of 2 to 4 helped us to reach contrast of $8\ 10^{-8}$ in narrow spectral bandwidth and $2\ 10^{-8}$ in monochromatic. We may expect better performance if we decrease the readout noise level or if we improve our minimization algorithm that is rather simple for now. More extensive chromatic tests must also be performed to estimate more precisely the overall performance of such an instrument on a telescope.

References

1. Marois, C. et al., Science, **322**, (2008) 1348
2. Lagrange, A.-M., et al., Astronomy and Astrophysics, **493**, (2009) L21
3. Beuzit, J.-L., et al., SPIE Proc., **7014** (2008) 701418
4. Macintosh, B., et al., SPIE Proc., **7015** (2008) 701518
5. Baudoz, P., et al., SPIE Proc., **7736** (2010) 77365S
6. Galicher, R., et al., Astronomy and Astrophysics, **509**, (2010) id.A31
7. Baudoz, P., et al., Proc. of IAU Colloq. 200, (2006) 553
8. Galicher, R., et al., Astronomy and Astrophysics, **488**, (2008) L9
9. Rouan, D., et al., PASP, **112**, (2000) 1479
10. Mas, M., et al., SPIE Proc., **7735** (2010) 773566
11. Borde, P. & Traub, W., Astrophysical Journal, **638** (2006) 488
12. Perrin, M., et al., Astrophysical Journal, **596** (2003) 702
13. Baudoz, P., et al., Proc. of AO for ELT 2, (2011) 41
14. Baudoz, P., et al.,SPIE, **8446**, (2012) 84468C
15. Mazoyer, J., et al.,Astronomy and Astrophysics, **557**, (2013) A9
16. Pueyo, L., Applied Optics, **48**, (2009) 6296